

## Article

# Effect of Wide-Spectrum Pulsed Magnetic Field on Solidification Structure of Pure Al at Constant Flow Velocity

Yawei Sun <sup>1</sup>, Bohuai Yao <sup>1</sup>, Zhen Zhao <sup>1</sup> and Yongyong Gong <sup>1,2,\*</sup><sup>1</sup> College of Science, Shanghai University, 99 Shangda Road, Shanghai 200444, China<sup>2</sup> Center for Advanced Solidification, Shanghai University, 99 Shangda Road, Shanghai 200444, China

\* Correspondence: gyy@shu.edu.cn

**Abstract:** The electromagnetic force generated by a pulsed magnetic field within a metal melt leads to changes in the internal temperature and flow fields of the molten metal, thus improving the solidification of the metal structure. Using the combination of a solidification test, experimental simulation and theoretical analysis, this study simulated the distribution of both electromagnetic force and the flow field in a metal melt under wide-spectrum pulse conditions, and studied the influence of a wide-spectrum pulsed magnetic field on the solidification structure of pure aluminium with a constant flow velocity. The results of this study show that the structural refinement of the solidification of pure aluminium can be different, in spite of equal flow velocity. Furthermore, this study shows that an applied time-averaged electromagnetic force causes crystal nuclei to pass through the solid–liquid interface boundary layer and promotes the growth of crystal grains. These grains flowed with the melt flow field to achieve both refinement and homogenization of the solidified structure.

**Keywords:** wide-spectrum pulsed magnetic field; equal flow velocity; industrial pure aluminium; grain refinement



**Citation:** Sun, Y.; Yao, B.; Zhao, Z.; Gong, Y. Effect of Wide-Spectrum Pulsed Magnetic Field on Solidification Structure of Pure Al at Constant Flow Velocity. *Metals* **2023**, *13*, 860. <https://doi.org/10.3390/met13050860>

Academic Editor: Jae Hong Shin

Received: 26 March 2023

Revised: 23 April 2023

Accepted: 24 April 2023

Published: 28 April 2023



**Copyright:** © 2023 by the authors. Licensee MDPI, Basel, Switzerland. This article is an open access article distributed under the terms and conditions of the Creative Commons Attribution (CC BY) license (<https://creativecommons.org/licenses/by/4.0/>).

## 1. Introduction

With the improvement of the concept of resources, energy and environment, high cleanliness and purification, high homogenization, ultra-fine crystallization, low consumption and low pollution have become the direction of the new generation of development for a new generation of steel metallurgy technology. The performance of a metal material ultimately depends on its structure. Moreover, the solidification process determines the overall structure of the metal to a great extent and therefore plays a major role in the performance of metal materials. Application of a pulsed electromagnetic field can refine the metal solidification structure and is an effective means to improve composition heterogeneity due to forced cooling during the casting process. Pulsed magnetic field fine-grain technology [1–6] has gradually attracted people’s attention due to its low energy consumption, remarkable effect, convenient application, strong universality and, at the same time, its ability to ensure the cleanliness of metals. Zi Bingtao et al. [7] studied the effect of both pulsed current and pulsed magnetic fields on the solidification structure of LY12 aluminium alloy and found that the treatment effect of a pulsed magnetic field on LY12 aluminium alloy was significantly better than that of pulsed current under the same control conditions. Bai Qingwei et al. [8] studied the effect of a pulsed electromagnetic field on the solidification structure of 7A04 aluminium alloy, and the results showed that a pulsed magnetic field can effectively produce spherical grains and a uniform microstructure in the alloy. Bao et al. [9] applied pulsed magnetic field (PMF) technology to an Al-Si-Mg-Cu-Ni alloy melt in the direct chill casting process, and found that the size of  $\alpha$ -Al and primary Si will be reduced after PMF treatment, while the distribution will be more uniform. Gong Yongyong et al. [10] discovered that the application of pulsed magnetic oscillation (PMO) during the nucleation stage and the first half of the nucleation growth can refine the structural solidification of

the metal, with crystal nuclei originating from the mould wall and the liquid surface of the melt. Edry et al. [11,12] applied a PMO treatment to pure aluminium (99.9% and 99.999% purity) and proposed a cavity crystal billet growth model. Cheng Shumin et al. [13,14] studied the effect of electromagnetic parameters on the refinement of a pure aluminium solidification structure with pure aluminium subjected to PMO with a constant input power. The study found that refinement of aluminium grains can be improved with an increase in current intensity. Wang Bin [15–17] and Fu Junwei et al. [18] found that a pulsed magnetic field can significantly reduce the size of various magnesium (Mg) alloys, leading to a transformation in Mg morphology from a dendritic shape to a spherical shape. Zhai Qijie et al. showed extensive results on the solidification structure of industrial pure aluminium [19–25], aluminium-copper alloys [26], 65 Mn steel [27] and GCr15 bearing steel [28] during the use of PMO and found that PMO can significantly improve the solidification structure, promote CET transformation and increase the equiaxed grain rate. Yin Zhenxing [19] proposed surface pulse magneto-oscillation (SPMO) technology and found that it has a refining effect on the solidification structure of pure aluminium, generating small equiaxed crystals inside the melt. Li Bo et al. [20] studied the effect of temperature field on the solidification structure of pure aluminium during PMO treatment and found that the combination of low frequency and high current can improve the refinement effect of the solidification structure. Gao et al. [29] studied the effect of a pulsed magnetic field on the solidification structure of pure aluminium. The study found that the grain refinement of the solidification structure is the result of the combined action of Lorentz force and Joule heat. Zhao Zhilong [30] studied the effect of pulse magnetic field on the solidification time of pure aluminium. The study found that applying a pulsed magnetic field can provide more nucleation energy, which is beneficial for increasing the nucleation rate. Zhao Jing et al. [31] studied the effect of different forms of coils on the solidification structure of pure aluminium and found that the grain size and proportion of equiaxed grain area are closely related to the electromagnetic effect of PMO. J.C. Jie et al. [32] applied a pulsed magnetic field to commercial pure aluminium to reveal nucleation and equiaxed crystal formation mechanisms. The results showed that the stronger Lorentz force acting on the solid grains pushes them towards the centre of the casting, increasing the nucleation number in the melt.

Kolesnichenko et al. [33] studied the relationship between the melt flow velocity and the current pulse width during a pulse and discovered an optimal pulse width to maximize the melt flow velocity. Le Qichi et al. [34,35] simulated the distribution of a magnetic field, flow field and temperature field in an electromagnetic DC casting during application of a pulsed magnetic field. The results of this study showed that the forced convection during application of the pulsed magnetic field can accelerate both melt movement and heat transfer. He Deping [36] et al. used a home-made Bridgman apparatus to introduce different interference growth waveforms during the Al-4%Mg dendrite process and discovered that different waveforms gradually enhanced the vibration interference of Al-4%Mg dendrite growth in sequence. Zhong Yuyi et al. [37] applied a pulse magnetic oscillation (abbreviated: PMO) waveform to pure aluminium and founded that the corresponding optimal pulse magnetic oscillation waveform changed with mould size. Zhang et al. [38] studied the effect of a pulsed magnetic field on the grain refinement of K4169 alloy and concluded that the combined effect of electromagnetic oscillation and melt convection caused by the pulsed magnetic field affected the grain refinement. Ban Chunyan et al. [39] concluded that the melt produced strong convection under the application of electromagnetic force, which led to the release of grains on the mould wall and an increase in the nucleation rate of the melt. Xu [40] investigated the intrinsic relationship between electromagnetic parameters and flow velocity and influenced the solidification of aluminium–silicon alloys by varying the pulse width of the electromagnetic field with constant current strength as well as period. The results showed that the maximum melt flow velocity corresponded to the best solidification structure refinement, which is considered to be the main cause of grain refinement.

It has been shown previously that a pulsed magnetic field can have a significant impact on all stages of liquid metal solidification, including the nucleation and growth of crystals, heat and mass transfer, and the solidification of the macrostructure. Therefore, the pulsed magnetic field is an effective way to improve solidification, metal morphology, and enhance application performance. The melt flow velocity is one of the most important factors influencing the refinement of the solidification structure of metals. In order to exclude the influence of the melt flow velocity on solidification experiment results for pure aluminium, a method was used that combined simulation and experimental verification to study the influence of a wide-spectrum pulsed magnetic field on the solidified structure of pure aluminium with a constant flow velocity. We add an isolation net on the liquid surface of the melt to avoid the formation of a large number of crystal nuclei due to the vibration of the liquid surface [10], in order to study the movement of crystal nuclei on the wall.

## 2. Numerical Simulation Model

### 2.1. Numerical Model

For this study, COMSOL multiphysics finite element software was used for experimental simulation to establish a two-dimensional axisymmetric mathematical model of an electromagnetic field with fluid flow coupling under a wide-spectrum pulsed magnetic field, as shown in Figure 1. The model includes a melt region (red), coil region (blue) and air region (grey). The dimensions of the melt and coil are consistent with the experimental results. The melt, coil and outermost air regions used structured (quadrilateral) grids, while the remaining air regions used unstructured (triangular) grids. The accuracy of this model has been verified [40] through comparing the measurement of the velocity of the melt using a Doppler velocimeter and the measurement of the magnetic field inside the melt using a Gaussian meter with numerical simulation results. The radius of the melt was 30.0 mm, and the height was 100.0 mm. Points A (29, 0), B (25, 0) and D (20, 0) were used to represent the distribution of electromagnetic forces within the melt, and point C (29, -40) was used to describe the flow velocity of the melt.

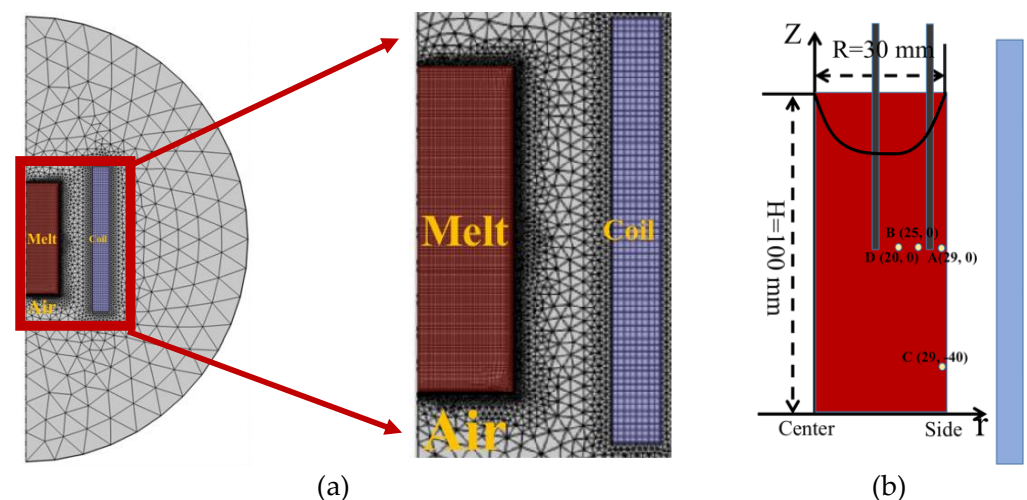


**Figure 1.** Numerical simulation model: (a) two-dimensional axisymmetric model; (b) geometric model.

The COMSOL multiphysics method is based on the finite element method and was used to solve the governing equations for both magnetic field and flow field. Furthermore, all aspects of the finite element mesh, including the melt, coil, mould, air region and infinite field must be taken into consideration. The relevant physical properties of industrial pure aluminium are shown in Table 1. Solidification under a pulsed magnetic field is a complex process, which allows for the following assumptions:

- (1) The solidification system is cylindrically symmetric, and a two-dimensional axisymmetric mathematical model is established to solve the coupling problem between the electromagnetic field and the fluid field.
- (2) The melt is considered to be an incompressible Newtonian fluid.
- (3) The model does not take into account the effect of Joule heat.
- (4) The effect of fluid flow on the magnetic field is neglected because the magnetic Reynolds number is significantly smaller than the unit.
- (5) The melt level does not oscillate.

**Table 1.** Physical performance parameters of industrial pure aluminium.

Parameter	Value
Density $\rho$ ( $\text{kg}\cdot\text{m}^{-3}$ )	2375
Liquidus temperature $T$ (K)	780
Electrical conductivity $\sigma_1$ ( $\text{S}\cdot\text{m}^{-1}$ )	$4.2 \times 10^6$
Magnetic conductivity $\sigma_s$ ( $\text{S}\cdot\text{m}^{-1}$ )	$9.09 \times 10^6$
Dynamic viscosity, $\mu$ ( $\text{Pa}\cdot\text{s}^{-1}$ )	$1.51 \times 10^{-3}$
Relative permittivity	1

The wide-spectrum pulse waveform was characterized by the presence of multiple pulses in a single cycle, and electromagnetic parameters such as pulse time interval ( $\tau_m$ ), pulse width ( $t$ ), current intensity ( $I$ ), period ( $T$ ) and wave number ( $n$ ) were adjusted. Changing any of these parameters affected the flow velocity of the melt. COMSOL multiphysics numerical simulation calculations were performed under conditions of constant pulse width and period and by continuously adjusting the electromagnetic combination parameters for the wave number and pulse time interval. The specific electromagnetic combination parameters obtained via simulation are shown in Table 2 ( $k_i$ ,  $k_t$ ,  $k_\tau$  are instrumentation parameters), and the corresponding waveform diagram is shown in Figure 2. In Figure 3, the velocity change at point C (29, -40) is shown with different electromagnetic combination parameters of both wave number and pulse time interval. The flow velocity at point C (29, -40) increased gradually with the number of pulse waves. Furthermore, during the intermittent period, the viscosity of the melt and dissipation of the turbulence gradually decreased the melt flow velocity. The flow velocity of the melt changed over time and reached the maximum value at multiple time points, which could not be compared. Therefore, a time average was taken for the flow velocity of the melt within one cycle to ensure that the time-average maximum flow velocity was equal. The simulation of the combined electromagnetic parameters for wave number and pulse time interval on the melt time-average flow velocity is shown in Figure 4. The flow field in the melt was distributed according to the law of double circulation. The flow direction of the upper circulation flowed clockwise, while the flow direction of the lower circulation flowed counterclockwise.

**Table 2.** Electromagnetic combination parameters of wave number and pulse time interval.

Group	Pulse Time Interval ( $\tau_m/\text{ms}$ )	Current Intensity (I/A)	Wave Number (n/N)	Pulse Width (t/ms)	Period (T/s)
untreated	-	-	-	-	-
Experimental group	5 $k_\tau$	2000 $k_i$	20	10 $k_\tau$	1.0 $k_t$
	6.7 $k_\tau$		16		
	10 $k_\tau$		12		
	15 $k_\tau$		12		
	20 $k_\tau$		14		

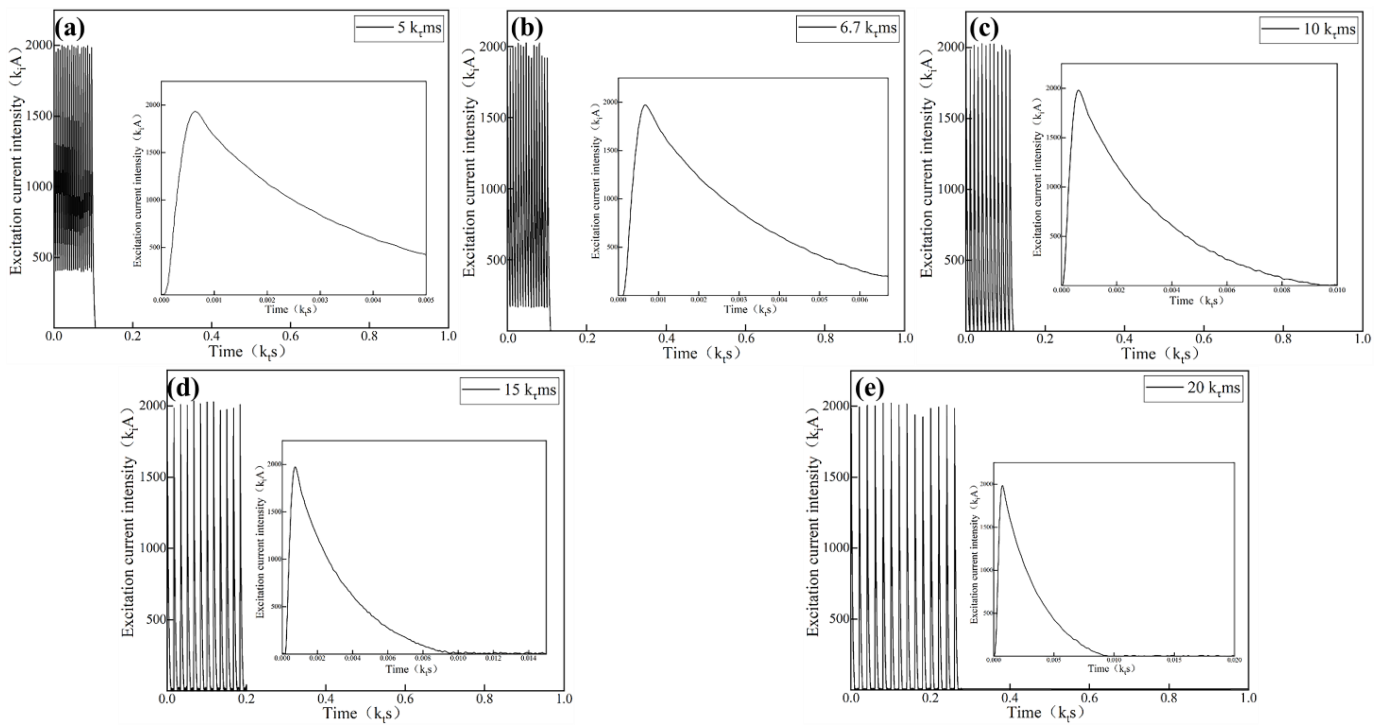


**Figure 2.** Schematic diagram of the waveform (a)  $\tau_m = 5 \text{ k}\tau\text{ms}$  &  $n = 20$ ; (b)  $\tau_m = 6.7 \text{ k}\tau\text{ms}$  &  $n = 16$ ; (c)  $\tau_m = 10 \text{ k}\tau\text{ms}$  &  $n = 12$ ; (d)  $\tau_m = 15 \text{ k}\tau\text{ms}$  &  $n = 12$ ; (e)  $\tau_m = 20 \text{ k}\tau\text{ms}$  &  $n = 14$ .

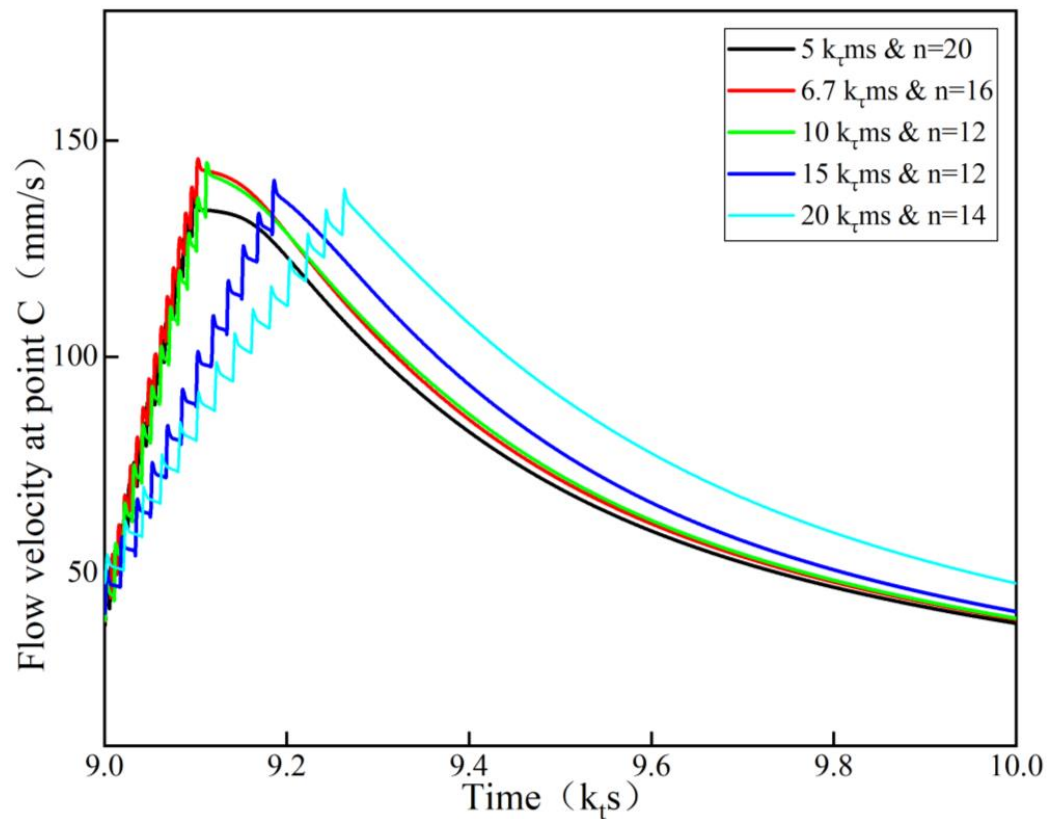


**Figure 3.** Variation of velocity at point C (29, -40) with time.

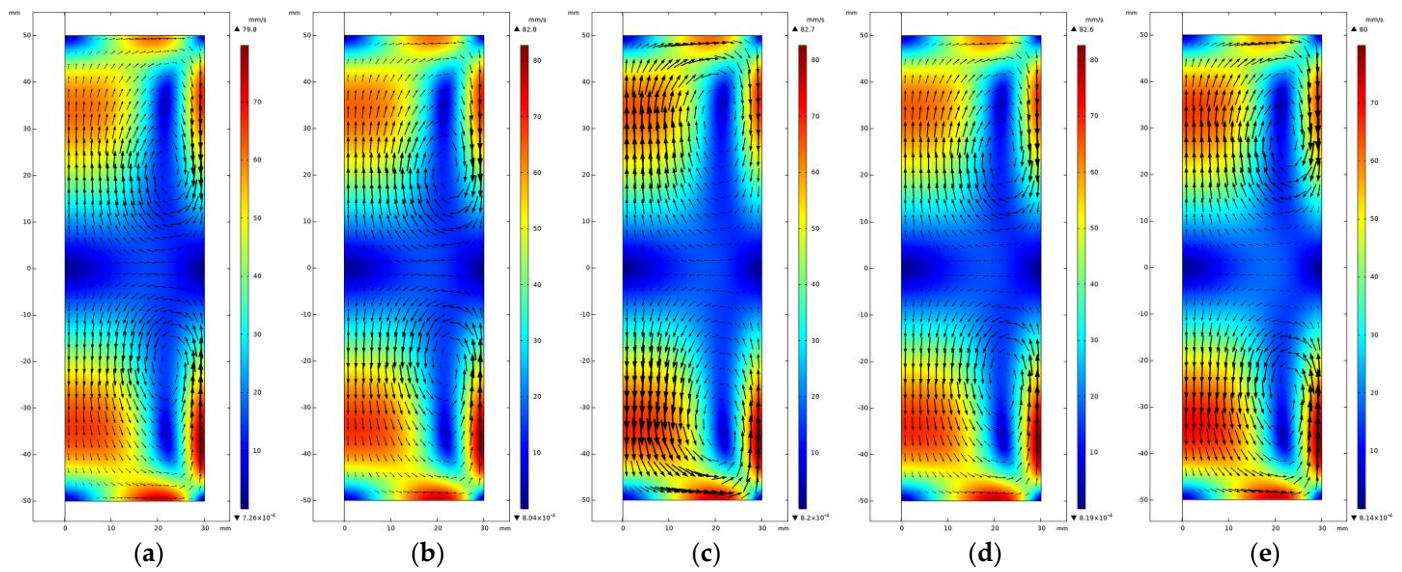


**Figure 4.** Distribution of the flow field within the melt: (a)  $\tau_m = 5 \text{ k}_\tau \text{ms}$  &  $n = 20$ ; (b)  $\tau_m = 6.7 \text{ k}_\tau \text{ms}$  &  $n = 16$ ; (c)  $\tau_m = 10 \text{ k}_\tau \text{ms}$  &  $n = 12$ ; (d)  $\tau_m = 15 \text{ k}_\tau \text{ms}$  &  $n = 12$ ; (e)  $\tau_m = 20 \text{ k}_\tau \text{ms}$  &  $n = 14$ .

## 2.2. Governing Equation

Using the Maxwell system of equations as the basis and starting point of finite element analysis, the differential equations are as follows:

$$\nabla \times E = -\frac{\partial B}{\partial t} \quad (1)$$

$$\nabla \times B = \frac{\partial D}{\partial t} + J \quad (2)$$

$$\nabla \cdot B = 0 \quad (3)$$

$$\nabla \cdot D = \rho_0 \quad (4)$$

where  $E$  is the electric field intensity vector,  $B$  is the magnetic flux density vector,  $D$  is the potential shift vector, and  $J$  is the current density vector and  $\rho_0$  is the charge density.

Corresponding constitutive equation:

$$J = \sigma E \quad (5)$$

$$B = \mu H \quad (6)$$

$$D = \epsilon_0 E \quad (7)$$

where  $\mu$  is permeability,  $\sigma$  is conductivity and  $\epsilon_0$  is the dielectric constant.

When the pulsed magnetic field is applied, the electromagnetic force density  $f$  generated by the interaction between the induced current  $J$  and the induced magnetic field  $B$  in the melt meets the formula:

$$f = J \times B \quad (8)$$

In the flow field analysis, the metal liquid is an incompressible Newtonian fluid; therefore, the melt movement can be formulated using the mass conservation continuous type equation and the N–S equation:

$$\nabla \cdot \mathbf{V} = 0 \quad (9)$$

$$\rho_l \left\{ \frac{\partial \mathbf{V}}{\partial t} + (\mathbf{V} \cdot \nabla) \mathbf{V} \right\} = -\nabla P + \eta \nabla^2 \mathbf{V} + F_V \quad (10)$$

where  $\rho_l$  is the liquid melt density,  $\mathbf{V}$  is the melt flow velocity,  $P$  is the pressure,  $\eta$  is the melt viscosity coefficient and  $F_V$  is the volume force.

### 3. Test Materials and Methods

The main test material in this study was industrial pure aluminium (99.7%), and the test equipment included in this study was as follows: a muffle furnace, stainless steel crucible, self-made coil (10 turns), oscilloscope, paperless recorder, thermocouple and wide-spectrum pulsed magnetic field charge–discharge device, among others. The solidification test device is shown in Figure 5.

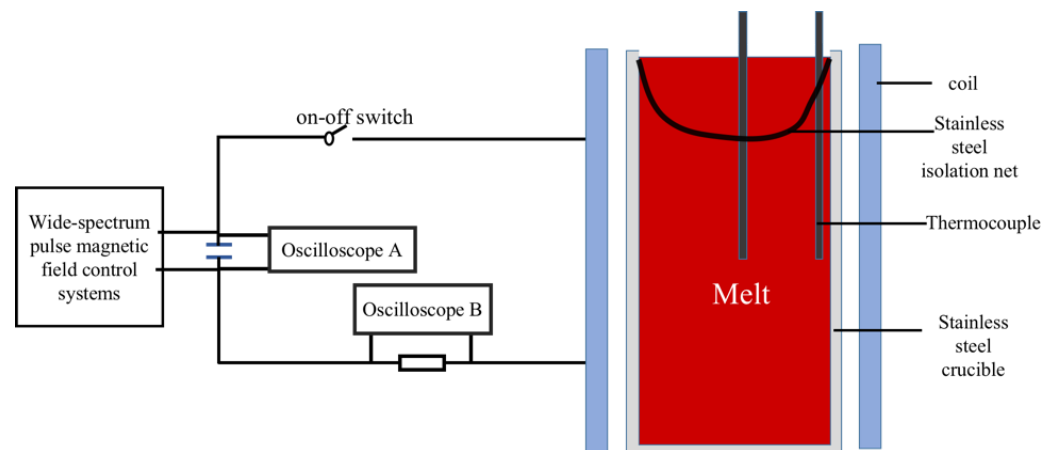


Figure 5. Schematic diagram of experimental apparatus.

The specific test method was performed as follows: industrial pure aluminium was placed in a corundum crucible, melted and heated to 780 °C in a resistance furnace. It was held for 30 min and subsequently slagged. The melt was poured into a stainless steel crucible ( $\Phi$  60 mm  $\times$  100 mm) and preheated to 700 °C with an isolation mesh, and a pulsed magnetic field was applied according to set parameters until complete solidification occurred and the temperature profile at solidification was measured. In order to study the movement of crystal nuclei generated on the mould wall, an isolation net was added to the liquid surface of the melt to avoid the formation of a large number of crystal nuclei due to the vibration of the liquid surface, which would have the potential to affect the experimental results. The obtained ingot was cut axially, and its section was polished with 400 mesh using laboratory sandpaper. The grain structure was corroded using a reagent with a composition ratio of HCl:HNO<sub>3</sub>:HF:H<sub>2</sub>O = 12:6:1:1, and the subsequent macrostructure was observed using the cross-sectional method to statistically analyse both the grain size and equiaxed grain area of the solid pure aluminium structure [41,42].

## 4. Results and Discussion

### 4.1. Experimental Result

In this study, the effect of electromagnetic combination parameters (wave number and pulse time interval) of a wide-spectrum pulsed magnetic field on the solidification of pure aluminium under the condition of constant flow velocity was investigated. The

vertical macroscopic illustration of pure aluminium is shown in Figure 6. As shown in Figure 6a, the solidification structure of pure aluminium without the application of a wide-spectrum pulsed magnetic field treatment consisted of a large number of coarse columnar crystals with a small number of equiaxed crystals at the bottom. Figure 6b–f shows what occurred when a wide-spectrum pulsed magnetic field was applied. In this case, a large number of fine equiaxed crystals were produced within the solidified structure, and the solidified structure of pure aluminium was refined. The percentage of area containing equiaxed crystals showed an increase followed by a decrease. The equiaxed crystal area ratio reached a maximum value of approximately 80% at  $n = 12$  &  $\tau_m = 10$  k $\tau$ -ms with a minimum equiaxed grain radius of 0.46 mm. The statistical results of the average grain size (black lines) and equiaxed grain area ratio (red lines) under the combined parameters of wave number and pulse time interval are shown in Figure 7.

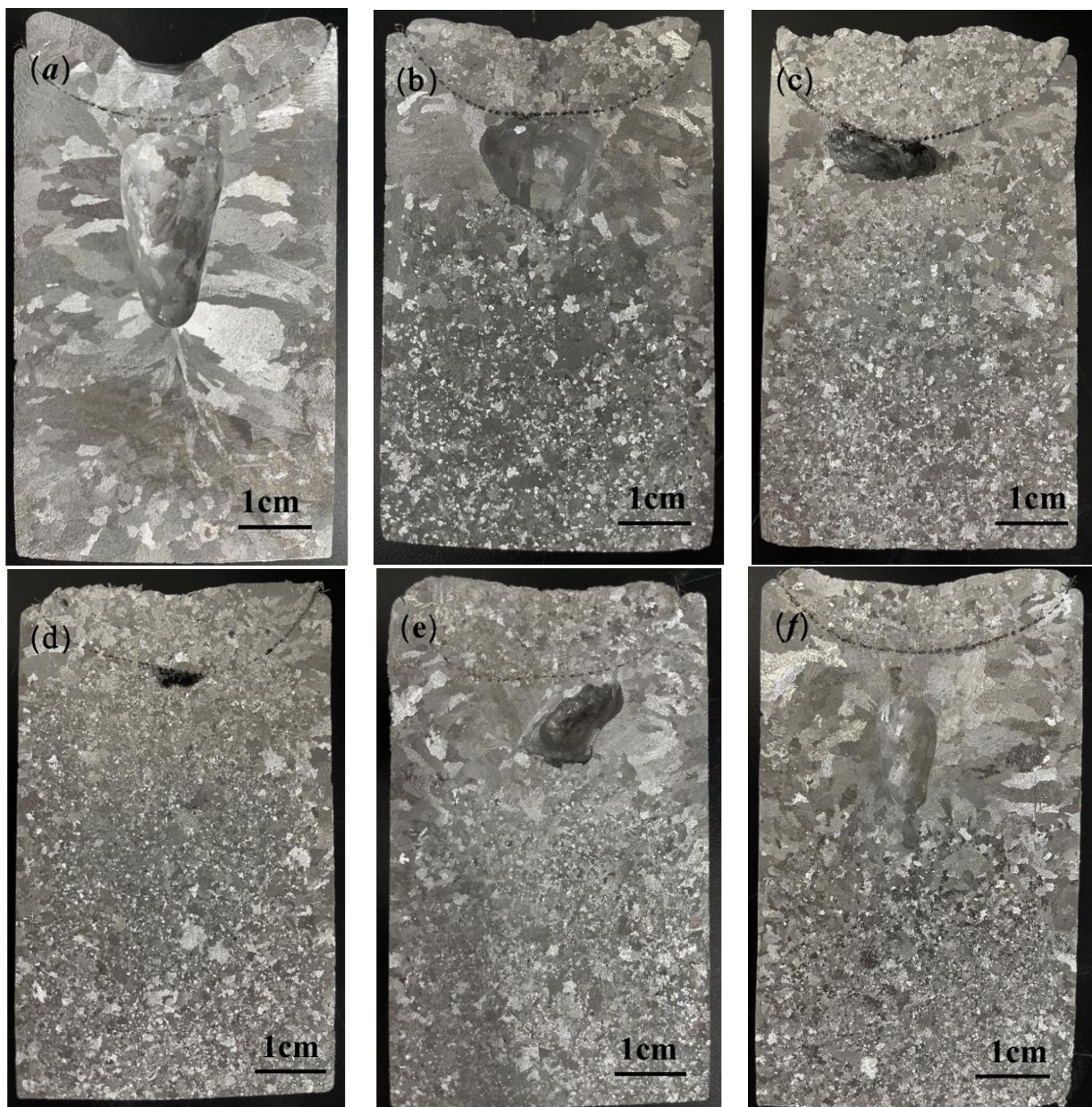


**Figure 6.** Longitudinal section macrostructure of industrial pure aluminium: (a) untreated; (b)  $\tau_m = 5$  k $\tau$ -ms &  $n = 20$ ; (c)  $\tau_m = 6.7$  k $\tau$ -ms &  $n = 16$ ; (d)  $\tau_m = 10$  k $\tau$ -ms &  $n = 12$ ; (e)  $\tau_m = 15$  k $\tau$ -ms &  $n = 12$ ; (f)  $\tau_m = 20$  k $\tau$ -ms &  $n = 14$ .

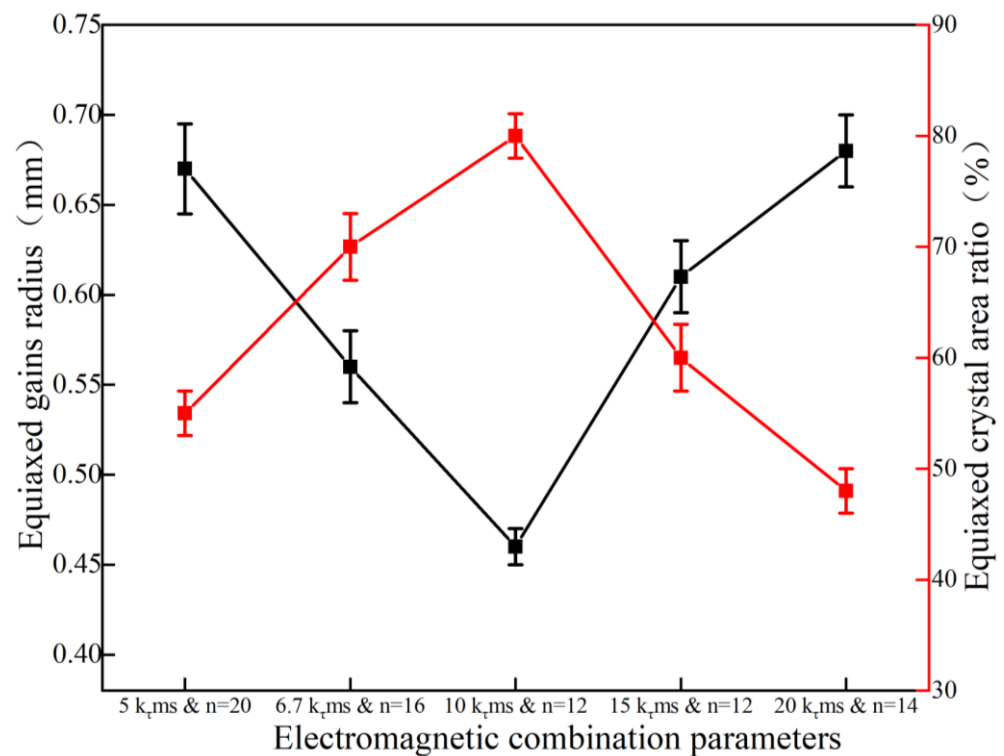


**Figure 7.** Statistical diagram of isoaxial crystal size and area percentage.

#### 4.2. Discussion and Analysis

Figure 8 shows radial electromagnetic force density changes over time for melt features point A (29, 0) subjected to electromagnetic combination parameters of both wave number and pulse time interval. As shown in Figure 8, the electromagnetic force in the -r direction was much greater than that of the +r direction (the electromagnetic force in the -r direction points towards the interior of the melt). In one cycle, the direction of the electromagnetic force changed many times, which was beneficial to the oscillation of the melt and allowed the crystal nuclei formed on the mould wall to fall off. The crystal nuclei moved across the solid–liquid interface to the centre and bottom of the melt due to the electromagnetic force. The nuclei moved with the flow field of the double-loop flow due to the forced convection of the melt, and eventually diffused to varying locations throughout it, eventually achieving homogeneous distribution. The cooling curve of the mould wall and centre during the process of metal solidification was measured, as shown in Figure 9. When pulse treatment was not applied, the temperature difference between the centre of the melt and the mould wall was significant. When pulse treatment was applied, the cooling curves at the centre of the melt and the mould wall were nearly identical. It is helpful to reduce the temperature gradient to reduce the central melt temperature to thus ensure a more uniform temperature distribution that is more conducive to the growth of equiaxed crystals from crystal nuclei. The time-average electromagnetic force density was obtained by averaging the electromagnetic force density of the pulse wave, the electromagnetic force extremes, and the time-averaged electromagnetic force density at point A (29, 0), as shown in Figure 10. The black line represents the extreme value of electromagnetic force density, while the red line represents the time-averaged electromagnetic force density. As the pulse time interval increased, the time-averaged electromagnetic force density increased and subsequently decreased, reaching a maximum value at  $n = 12$  &  $\tau_m = 10 k_{\tau}$ .ms.

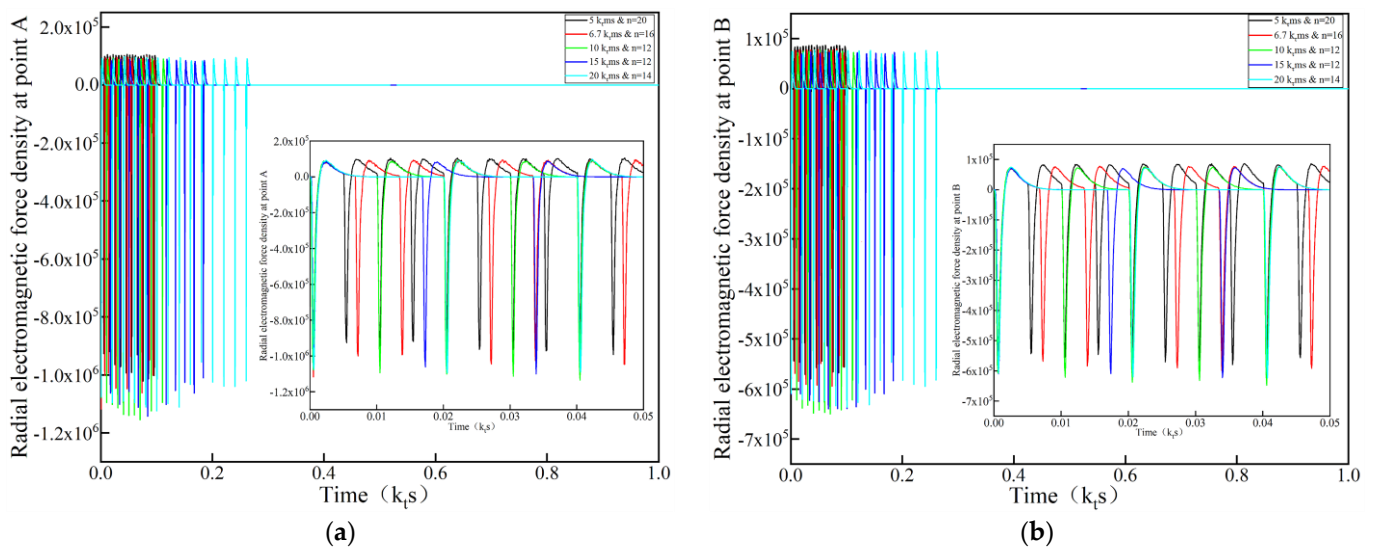


**Figure 8.** Distribution of radial electromagnetic force density at characteristic points with time: (a) electromagnetic force density at point A (29, 0) with time; (b) electromagnetic force density at point B (25, 0) with time.

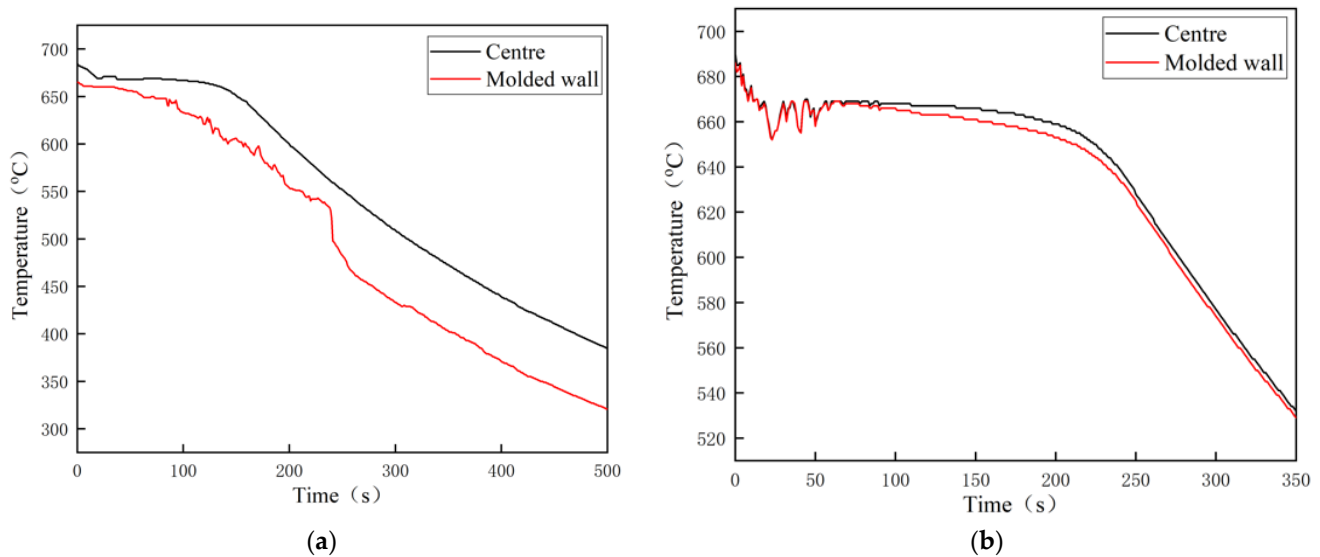


**Figure 9.** Cooling curve during solidification (a) solidification curve without treatment; (b) solidification curve with a broad spectrum pulsed magnetic field applied.

There was a dispersion effect in the propagation of electromagnetic waves in the metal melt. The higher the frequency, the faster the electromagnetic wave decayed during the propagation of metal. Therefore, high-frequency electromagnetic waves were generally distributed on the surface of the metal melt. The Fourier transform of the electromagnetic combined pulse waveform for both wave number and pulse time interval, as well as their spectrum distribution, are shown in Figure 11. The spectrum consists of discrete spectral lines, each representing a sine wave. The higher peaks corresponded to the fundamental frequency and integer multiples of the fundamental frequency, with each peak representing the dominant harmonic frequency component. The spectrum of the wide-spectrum pulsed magnetic field showed that, as the pulse interval increased, the frequency component of the field was dominated by lower harmonic frequencies. When the frequency components changed, the distribution of the electromagnetic force also changed. When the pulse time interval was  $5 k\tau_{ms}$  and  $6.7 k\tau_{ms}$ , the fundamental frequency was higher after fast Fourier transform, while the electromagnetic force in the melt attenuated quickly due to the skin

effect. As the pulse time interval increases, the fundamental frequency is lower and the spectrum is more abundant after fast Fourier transform. Figure 12 shows the extreme values of electromagnetic force at points A (29, 0), B (25, 0), and C (20, 0) under the combination of wave number and pulse time interval. The electromagnetic force decays within the melt, and the high-frequency component decays faster.

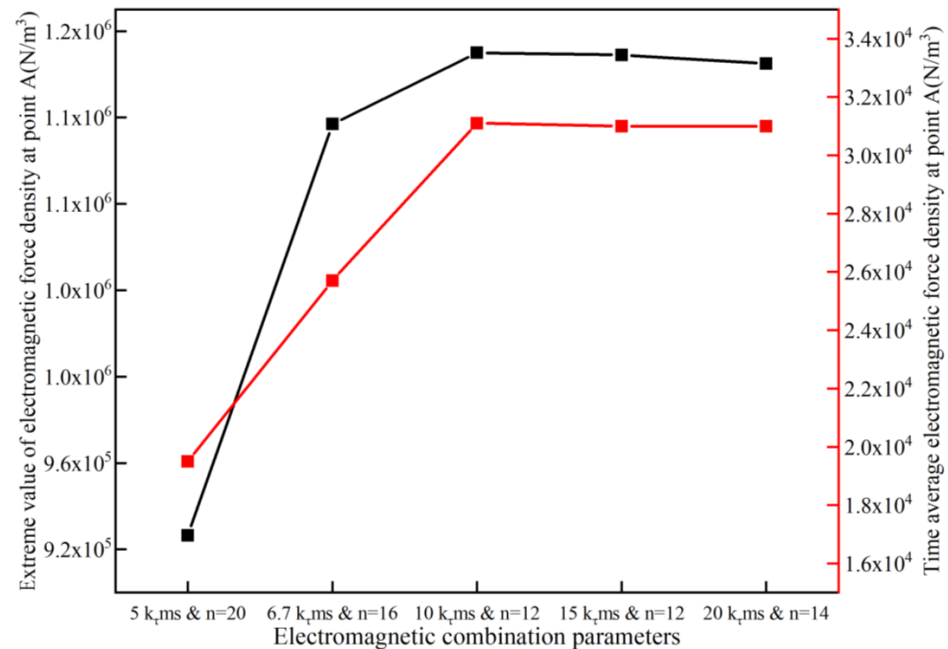


**Figure 10.** Extreme and time-averaged electromagnetic force density at point A (29, 0) for different combinations of electromagnetic parameters.

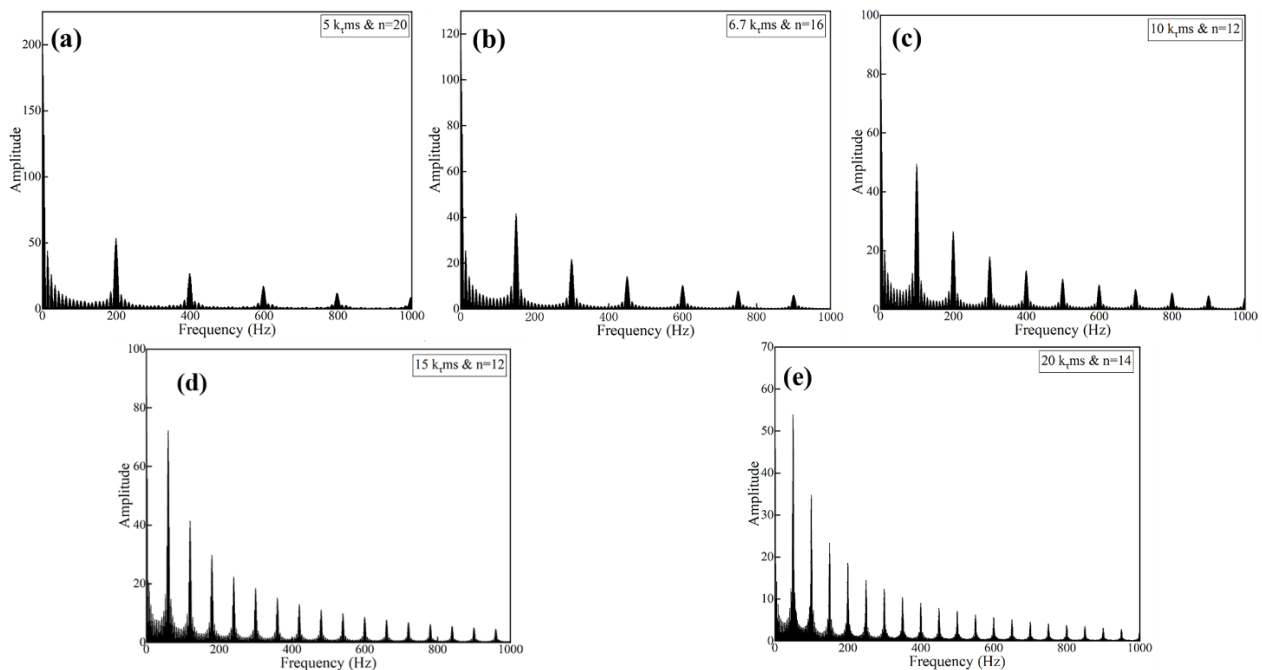


**Figure 11.** Spectrum of wide-spectrum pulse waveform for different pulse intervals: (a)  $\tau_m = 5 k_{\tau}$ .ms &  $n = 20$ ; (b)  $\tau_m = 6.7 k_{\tau}$ .ms &  $n = 16$ ; (c)  $\tau_m = 10 k_{\tau}$ .ms &  $n = 12$ ; (d)  $\tau_m = 15 k_{\tau}$ .ms &  $n = 12$ ; (e)  $\tau_m = 20 k_{\tau}$ .ms &  $n = 14$ .

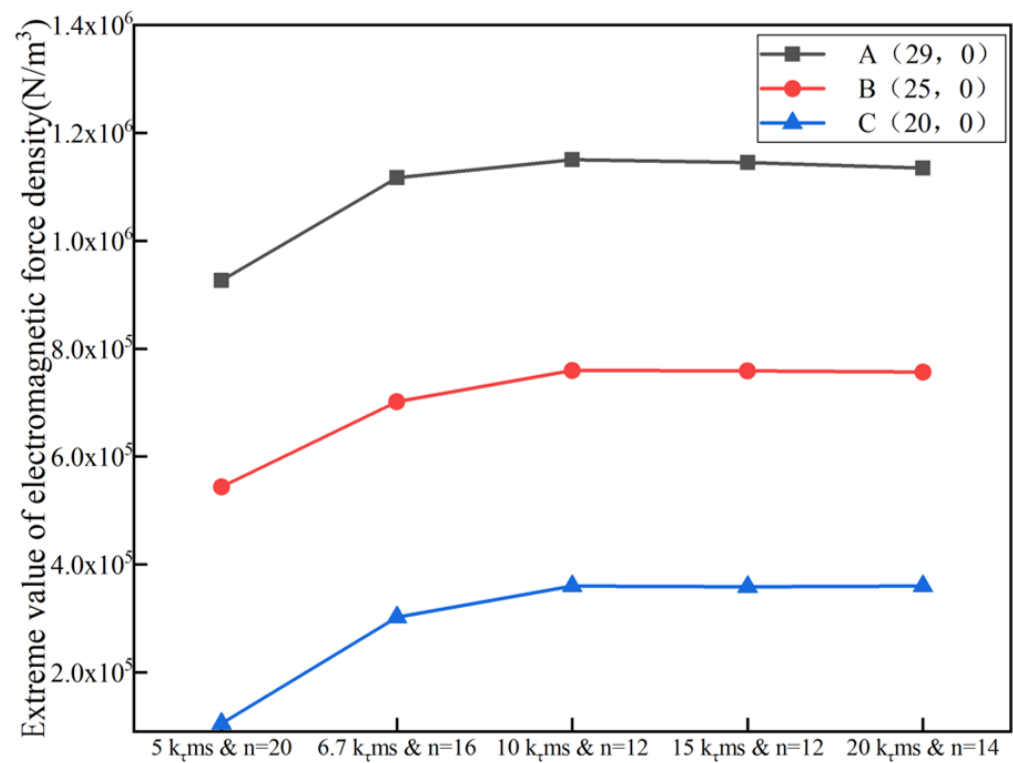


**Figure 12.** Extreme values of electromagnetic force at points A (29, 0), B (25, 0), and C (20, 0).

Movement of the crystal nuclei had a significant effect on homogenization of the solidified structure. Melt flow is created by the electromagnetic force generated by the interaction of the electromagnetic field and induced current in the melt. The flow velocity of the melt at the solid–liquid interface was almost zero. When only the radial movement of the crystal nucleus was considered, the crystal nuclei moved due to electromagnetic force in the radial direction, as well as viscous force. This can be simplified as follows: the crystal nuclei were regarded as spheres; the crystal nuclei at the solid–liquid interface were not affected by melt flow; the radial motion of the crystal nuclei was the main consideration; the crystal nuclei were mainly located in the mould wall.

Electromagnetic force density of spherical crystal nuclei:

$$f_n = (J \times B) \left( \frac{\sigma_s}{\sigma_l} - 1 \right) \quad (11)$$

Electromagnetic force on spherical crystal nuclei:

$$F = \frac{4}{3} \pi r^3 f_n \quad (12)$$

Viscous force of spherical crystal nuclei:

$$F_v = 6\pi\eta r v \quad (13)$$

where  $\eta$  is the viscosity coefficient of the melt,  $r$  is the radius of crystal nuclei,  $v$  is the radial velocity of the crystal nuclei,  $\sigma_l$  is the liquid phase conductivity and  $\sigma_s$  is the solid phase conductivity.

Pulse time interval  $\tau_m$  is pulse time  $t_n$  and pulse intermission time  $t_m$ .

$$\tau_m = t_n + t_m \quad (14)$$

Since the electromagnetic force changes periodically, the crystal nuclei accelerate their movement within a pulse time, and the average electromagnetic force within a pulse time is expressed as:

$$\bar{F} = \frac{\int_0^{t_n} F dt}{t_n} = \frac{4}{3} \pi r^3 \bar{f}_n \quad (15)$$

The electromagnetic force and viscous force acting on the spherical crystal nuclei meet the momentum theorem:

$$m \frac{dv}{dt} = \bar{F} - 6\pi\eta r v \quad (16)$$

where  $m = \frac{4}{3}\rho\pi r^3$ ,  $\rho$  is the density of crystal nuclei,  $\tau$  is the time of electromagnetic force action and the formula of crystal nuclei velocity is obtained by combining Formulas (11)–(14):

$$v = \frac{2r^2\bar{f}_n}{9\eta} \left( 1 - e^{-\frac{9\eta}{2r^2\rho}t} \right) \quad (17)$$

Due to the small size of the crystal nuclei, the crystal nuclei quickly reaches the maximum value under the action of electromagnetic force, and the Formula (17) is simplified:

$$v = \frac{2r^2\bar{f}_n}{9\eta} \quad (18)$$

The total average displacement can be expressed as:

$$\bar{x} = nv \cdot t_n \quad (19)$$

The thickness of the boundary layer at the solid–liquid interface is  $\delta_0$ ,  $L$  is the characteristic length of the melt, which is related to the size of the melt.  $v_l$  is the velocity of the melt,  $\rho_l$  is the density of the metal melt, the advancing speed of solid–liquid interface is  $v_{ls}$  and this solid–liquid interface boundary layer advances during the pulse intermission time  $t_m$ . Then, the recommended law of boundary layer meets:

$$\delta_0 = \frac{5L}{\sqrt{Re}} \quad (20)$$

$$Re = \frac{\rho_l v_l L}{\eta} \quad (21)$$

$$\delta = \delta_0 + v_{ls} t_m \quad (22)$$

Critical conditions for crystal nuclei to cross boundary layer:

$$\bar{x} \geq \delta \quad (23)$$

Based on the above formula, the relationship satisfied by each variable is obtained:

$$r \geq \sqrt{\frac{9\eta(\delta_0 + v_{ls}t_m)}{2nt_n\bar{f}_n}} \quad (24)$$

$$n > \frac{9\eta(\delta_0 + v_{ls}t_m)}{2r^2t_n\bar{f}_n} \quad (25)$$

Given the existence of a velocity boundary layer at the solid–liquid interface, the viscosity of the velocity boundary layer was higher than that of the liquid melt; thus, the melt flowed slowly, and as a result it was very difficult for the nuclei to enter the interior of the melt by flow only. Due to different solid–liquid conductivity, the nuclei move relative to the melt under the pulsed electromagnetic force. The nuclei crossed the boundary layer and entered the interior of the melt due to the electromagnetic force. As

the radius of the crystal nuclei entering the melt from the solid–liquid interface boundary layer became smaller, more crystal nuclei entered the melt, which led to higher refinement of the solidified structure. According to Equation (18), when the electromagnetic force density is constant, it is easier for larger nuclei to cross the boundary layer and enter the melt with greater velocity. It is shown from Equation (25) that when the pulse time interval ( $\tau_m$ ) was less than the pulse width ( $t$ ), the pulse intermission time ( $t_m$ ) was zone. Therefore, a larger average electromagnetic force leads to the necessity of fewer waves for crystal nuclei with the same radius to cross the boundary layer of the solid–liquid interface. When the pulse time interval ( $\tau_m$ ) was greater than pulse width ( $t$ ), the solid–liquid interface boundary layer advanced during the pulse intermission time ( $t_m$ ). Therefore, a large pulse intermission time ( $t_m$ ) requires a large pulse wave number for crystals with the same radius to cross the solid–liquid interface boundary layer under the same electromagnetic force.

## 5. Conclusions

In this study, the influence of electromagnetic combination parameters (wave number and pulse time interval) of a wide-spectrum pulsed magnetic field with constant flow velocity was studied for their effects on the solidification structure of pure aluminium. The conclusions from this study are as follows:

- (1) The solidification refinement effect of industrial pure aluminium was different with regard to equal time-averaged maximum flow velocity of the melt when changes were made to the electromagnetic combination parameters of the wide-spectrum pulsed magnetic field.
- (2) The frequency component of the wide-spectrum pulsed magnetic field changed, as did the distribution of the electromagnetic force in the melt. When the pulse time interval was smaller than the pulse width, the combination of wave number and pulse time interval ensured equal melt flow velocity. As the pulse time interval increases, the refinement effect of pure aluminium solidification structure becomes more obvious.
- (3) Numerical simulation results showed that the flow velocity did not change significantly when the pulse time interval was greater than the pulse width, and was determined to be approximately equal. The experimental results of the study indicate that, when the pulse time interval is greater than the pulse width, the refinement effect of the pure aluminium solidification structure deteriorates as the pulse time interval increases.

**Author Contributions:** Conceptualization, Y.G.; investigation, B.Y.; resources, Z.Z.; writing—review and editing, Y.S. All authors have read and agreed to the published version of the manuscript.

**Funding:** National Natural Science Fund Project (52071194); National Key Research and Development (R & D) Program Supported Project (2020YFB2008401).

**Data Availability Statement:** Not applicable.

**Conflicts of Interest:** The authors declare no conflict of interest.

## References

1. Wang, D.; Li, H.Q.; Zhang, X.L.; Ding, P.; Deng, Y.F. The influence of pulse magnetic field intensity on the morphology and electrochemical properties of NiCoS alloys. *Surf. Coat. Technol.* **2020**, *403*, 126406. [[CrossRef](#)]
2. Duan, W.; Yin, S.; Liu, W.; Zhao, Z.; Hu, K.; Wang, P.; Cui, J.; Zhang, Z. Numerical and experimental studies on solidification of AZ80 magnesium alloy under out-of-phase pulsed magnetic field. *J. Magnes. Alloy.* **2021**, *9*, 166–182. [[CrossRef](#)]
3. Li, L.; Liang, W.; Ban, C.Y.; Suo, Y.; Lv, G.; Liu, T.; Wang, X.; Zhang, H.; Cui, J. Effects of a high-voltage pulsed magnetic field on the solidification structures of biodegradable Zn–Ag alloys. *Mater. Charact.* **2020**, *163*, 110274. [[CrossRef](#)]
4. Teng, Y.F.; Li, Y.J.; Feng, X.F.; Yang, Y. Effect of rectangle aspect ratio on grain refinement of superalloy k4169 under pulsed magnetic field. *Acta. Metall. Sin.* **2015**, *51*, 844.
5. Zhang, Y.H.; Zhong, H.G.; Zhai, Q.J. Research progress of grain refinement and homogenization of solidified metal alloys driven by pulsed electromagnetic fields. *J. Iron Steel Res.* **2017**, *29*, 249.
6. Yunpeng, Z.; Li, S.; Yanfei, F.; Shunqing, X.; Yonglin, M. Effect of Surface Pulse Magnetic Field on the Solidification Process of 7A04 Aluminum Alloy. *Therm. Process. Technol.* **2021**, *50*, 56–63.

7. Bingtao, Z.; Jianzhong, C.; Qixian, B. Comparison of solidification structure of LY12 aluminum alloy under the action of pulsed current and pulsed magnetic field. *Hot Working Process* **2000**, *4*, 3.
8. Xinyu, B.; Jun, W.; Qingwei, B.; Weiwei, F.; Cunlei, Y.; Yongling, M. Effect of pulsed electromagnetic energy on the refining mechanism of solidification structure of 7A04 aluminum alloy. *J. Mater. Heat Treat.* **2019**, *5*, 7.
9. Bao, X.; Ma, Y.; Xing, S.; Liu, Y.; Shi, W. Effects of pulsed magnetic field melt treatment on grain refinement of Al-Si-Mg-Cu-Ni alloy direct-chill casting billet. *Metals* **2022**, *12*, 1080. [[CrossRef](#)]
10. Gong, Y.-Y.; Luo, J.; Jing, J.-X.; Xia, Z.-Q.; Zhai, Q.-J. Structure refinement of pure aluminum by pulse magneto-oscillation. *Mater. Sci. Eng. A* **2008**, *497*, 147–152. [[CrossRef](#)]
11. Edry, I.; Erukhimovitch, V.; Shoihet, A.; Mordekovitz, Y.; Frage, N.; Hayun, S. Effect of impurity levels on the structure of solidified aluminum under pulse magneto-oscillation (PMO). *J. Mater. Sci.* **2013**, *48*, 8438–8442. [[CrossRef](#)]
12. Edry, I.; Frage, N.; Hayun, S. The effect of pulse magneto-oscillation treatment on the structure of aluminum solidified under controlled convection. *Mater. Lett.* **2016**, *182*, 118–120. [[CrossRef](#)]
13. Gong, Y.Y.; Cheng, S.-M.; Zhong, Y.-Y.; Wang, X.; Zhang, Y.-H.; Zhai, Q.-J.; Zhong, H.-G.; Xu, Z.-S.; Yue, R.; Pei, N. Influence of electromagnetic parameters on solidification structure of pure Al in the case of identical power. *J. Iron Steel Res. Int.* **2018**, *25*, 854–861. [[CrossRef](#)]
14. Cheng, S.; Zhong, Y.; Xu, Z.; Pei, N.; Zhai, Q.; Gong, Y.Y. Effect of flow on solidification structure of pure aluminium under pulse magneto-oscillation. *Mater. Sci. Technol.* **2018**, *34*, 1212–1217. [[CrossRef](#)]
15. Wang, B. Microstructure refinement of AZ91D alloy solidified with pulsed magnetic field. *Trans. Nonferrous Met. Soc. China* **2008**, *13*, 536–540. [[CrossRef](#)]
16. Wang, B.; Yang, Y.S.; Sun, M.L. Microstructure refinement of AZ31 alloy solidified with pulsed magnetic field. *Trans. Nonferrous Met. Soc. China* **2010**, *20*, 1685–1690. [[CrossRef](#)]
17. Wang, B.; Yang, Y.S.; Zhou, J.X.; Tong, W.H. Structure refinement of pure Mg under pulsed magnetic field. *Mater. Sci. Technol.* **2011**, *27*, 176–179. [[CrossRef](#)]
18. Fu, J.W.; Yang, Y.S. Microstructure and mechanical properties of Mg-Al-Zn alloy under a low-voltage pulsed magnetic field. *Mater. Lett.* **2012**, *67*, 252–255. [[CrossRef](#)]
19. Yin, Z.-X.; Gong, Y.-Y.; Li, B.; Cheng, Y.-F.; Liang, D.; Zhai, Q.-J. Refining of pure aluminum cast structure by surface pulsed magneto-oscillation. *J. Mater. Process. Technol.* **2012**, *212*, 2629–2634. [[CrossRef](#)]
20. Bo, L.; Yin, Z.; Gong, Y.; Li, R.; Zhai, Q. Effect of pouring temperature on refining the solidification structure of pure aluminum by pulsed magnetic oscillation. *J. Shanghai Univ. Nat. Sci. Ed.* **2012**, *18*, 323–326.
21. Dong, L.; Liang, Z.; Zhai, Q.; Wang, G.; StJohn, D.H. Nucleation and grain formation of pure Al under Pulsed Magneto-Oscillation treatment. *Mater. Lett.* **2014**, *130*, 48–50.
22. Li, Q.; Yu, J.; Liang, D.; Zhang, Z.; Gong, Y. Study on the mechanism of refining industrial pure aluminum by pulsed magnetic oscillation. *Shanghai Met.* **2015**, *37*, 4.
23. Zhao, J.; Cheng, Y.; Han, K.; Zhang, X.; Xu, Z.; Zhai, Q. Numerical and experimental studies of surface—Pulsed magnetic-oscillation on solidification. *J. Mater. Process. Technol.* **2016**, *229*, 286. [[CrossRef](#)]
24. Dong, L.; Sun, J.; Liu, T.; Zhai, Q.; Wang, G.; StJohn, D.H.; Dong, H.; Zhong, H. Enhanced Heterogeneous Nucleation by Pulsed Magnetic-Oscillation Treatment of Liquid Aluminum Containing Al<sub>3</sub>Ti<sub>1</sub>B Additions. *Adv. Eng. Mater.* **2015**, *17*, 1465–1469.
25. Zhao, J.; Yu, J.; Li, Q.; Zhong, H.; Song, C.; Zhai, Q. Structure of slowly solidified <sup>30</sup>Cr<sub>2</sub>Ni<sub>4</sub>MoV casting with surface pulsed magneto-oscillation. *Mater. Sci. Technol.* **2015**, *31*, 1589. [[CrossRef](#)]
26. Xu, Z.; Li, Q.; Liang, Z.; Zhai, Q.; Gong, Y. Microstructural morphology of an Al-4.5wt% Cu alloy under pulsed magnetic oscillation. *Shanghai Met.* **2015**, *37*, 5.
27. Cao, T.; Zhai, Q.; Li, R.; Zhang, J.; Chen, J. Effect of Magnetically Induced Oscillation on the Internal Structure of 65Mn Steel Ingots. *Iron Steel Res.* **2014**, *6*, 6.
28. Cheng, Y.; Xu, Z.; Zhou, Z.; Xu, Y.; Huang, Z.; Zhong, H. Application of PMO solidification homogenization technology in the production of continuous casting GCr15 bearing steel. *Shanghai Met.* **2016**, *38*, 4.
29. Gao, Y.-L.; Li, Q.-S.; Gong, Y.-Y.; Zhai, Q.-J. Comparative study on structural transformation of low-melting pure Al and high-melting stainless steel under external pulsed magnetic field. *Mater. Lett.* **2007**, *61*, 4011–4014. [[CrossRef](#)]
30. Zhao, Z.L.; Liu, Y.; Liu, L. Grain refinement induced by a pulsed magnetic field and synchronous solidification. *Mater. Manuf. Process.* **2011**, *26*, 1202–1206. [[CrossRef](#)]
31. Zhao, J.; Xu, Z.S. Numerical simulation of electromagnetic, flow and temperature distribution during ingot solidification process under HPMO. *Shanghai Met.* **2018**, *40*, 90–94.
32. Jie, J.C.; Yue, S.P.; Liu, J.; StJohn, D.H.; Zhang, Y.B.; Guo, E.Y.; Wang, T.M.; Li, T.J. Revealing the mechanisms for the nucleation and formation of equiaxed grains in commercial purity aluminum by fluid-solid coupling induced by a pulsed magnetic field. *Acta Mater.* **2021**, *208*, 116747. [[CrossRef](#)]
33. Kolesnichenko, A.F.; Podoltsev, A.D.; Kucheryavaya, I.N. Action of Pulse Magnetic Field on Molten Metal. *ISIJ Int.* **1994**, *34*, 715–721. [[CrossRef](#)]
34. Jia, Y.; Wang, H.; Le, Q. Transient coupling simulation of multi-physical field during pulse electromagnetic direct-chill casting of AZ80 magnesium alloy. *Int. J. Heat Mass Transf.* **2019**, *143*, 118524. [[CrossRef](#)]

35. Wang, H.; Jia, Y.; Le, Q.; Bao, L. Transient numerical simulation of solidification characteristic under differential phase pulsed magnetic field. *Comput. Mater. Sci.* **2020**, *172*, 109261. [[CrossRef](#)]
36. He, D.; Chen, F.; Shu, G. Effect of vibration interference waveform on dendritic growth. *J. Artif. Lenses* **1989**, *18*, 262–266.
37. Zhong, Y.; Bai, Y.; Li, G.; Gong, Y.; Zhai, Q. Effect of pulsed magnetic oscillation waveform on solidification structure of pure aluminum. *Shanghai Met.* **2021**, *43*, 92–97.
38. Zhang, K.L.; Li, Y.J.; Yang, Y.S. Simulation of the influence of pulsed magnetic field on the superalloy melt with the solid–liquid interface in directional solidification. *Acta Metall. Sin. (Engl. Lett.)* **2020**, *33*, 1442. [[CrossRef](#)]
39. Ban, C.; Cui, J.; Ba, Q.; Lu, G.; Zhang, B. Effect of pulsed magnetic field on the microstructure of LY12 aluminum alloy. *Spec. Cast. Non Ferr. Alloy.* **2004**, *5*, 12–15.
40. Xu, Y.; Zhang, Y.; Zheng, T.; Gong, Y.; Song, C.; Zheng, H.; Zhai, Q. Evolution of melt convection in a liquid metal driven by a pulsed electric current. *Chin. Phys. B* **2021**, *30*, 495–503. [[CrossRef](#)]
41. *ASTM STP 839; Grain Size Measurement*. American Society for Testing and Materials: West Conshohocken, PA, USA, 1984.
42. Wei, X. Discussion on the Area Method and the Cut Line Method for Determining the Number of Grain Per Unit Area on a Polished Metal Surface. *Phys. Test.* **1989**, *2*, 55–60.

**Disclaimer/Publisher’s Note:** The statements, opinions and data contained in all publications are solely those of the individual author(s) and contributor(s) and not of MDPI and/or the editor(s). MDPI and/or the editor(s) disclaim responsibility for any injury to people or property resulting from any ideas, methods, instructions or products referred to in the content.